

Cite this: *Chem. Sci.*, 2022, 13, 8829

All publication charges for this article have been paid for by the Royal Society of Chemistry

# SrO-layer insertion in Ruddlesden–Popper Sn-based perovskite enables efficient CO<sub>2</sub> electroreduction towards formate†

Jing Zhao,<sup>†ab</sup> Peng Zhang,<sup>†ab</sup> Lulu Li,<sup>ab</sup> Tenghui Yuan,<sup>ab</sup> Hui Gao,<sup>ab</sup> Gong Zhang,<sup>ab</sup> Tuo Wang,<sup>ab</sup> Zhi-Jian Zhao<sup>ab</sup> and Jinlong Gong<sup>ab</sup>\*

Tin (Sn)-based oxides have been proved to be promising catalysts for the electrochemical CO<sub>2</sub> reduction reaction (CO<sub>2</sub>RR) to formate (HCOO<sup>-</sup>). However, their performance is limited by their reductive transformation into metallic derivatives during the cathodic reaction. This paper describes the catalytic chemistry of a Sr<sub>2</sub>SnO<sub>4</sub> electrocatalyst with a Ruddlesden–Popper (RP) perovskite structure for the CO<sub>2</sub>RR. The Sr<sub>2</sub>SnO<sub>4</sub> electrocatalyst exhibits a faradaic efficiency of 83.7% for HCOO<sup>-</sup> at -1.08 V vs. the reversible hydrogen electrode with stability for over 24 h. The insertion of the SrO-layer in the RP structure of Sr<sub>2</sub>SnO<sub>4</sub> leads to a change in the filling status of the anti-bonding orbitals of the Sn active sites, which optimizes the binding energy of \*OCHO and results in high selectivity for HCOO<sup>-</sup>. At the same time, the interlayer interaction between interfacial octahedral layers and the SrO-layers makes the crystalline structure stable during the CO<sub>2</sub>RR. This study would provide fundamental guidelines for the exploration of perovskite-based electrocatalysts to achieve consistently high selectivity in the CO<sub>2</sub>RR.

Received 1st June 2022

Accepted 28th June 2022

DOI: 10.1039/d2sc03066g

rsc.li/chemical-science

## Introduction

The electrochemical CO<sub>2</sub> reduction reaction (CO<sub>2</sub>RR) is an attractive and sustainable approach to mitigate the greenhouse effect by storing renewable energy (*e.g.*, solar and wind energy) in the form of chemical bonds.<sup>1–3</sup> The CO<sub>2</sub>RR can yield a variety of valuable products, among which formate (HCOO<sup>-</sup>) shows the advantages of environmental compatibility and transportability as an important raw material.<sup>4,5</sup> It is also a promising material for liquid hydrogen storage for fuel cell applications.<sup>5,6</sup> HCOO<sup>-</sup> production by the CO<sub>2</sub>RR has been proved to be predominately realized by tin(Sn)-based electrocatalysts.<sup>7–12</sup> The emerging evidence suggested that Sn oxides exhibit high activity.<sup>7,13</sup> Besides, Sn-based electrocatalysts have the advantages of low cost, abundance in the earth's crust and environmental friendliness.<sup>7–9</sup> Nevertheless, their selectivity to HCOO<sup>-</sup> would drop with the proceeding of the CO<sub>2</sub>RR due to their reductive transformation into metallic derivatives.<sup>14,15</sup> Thence, there is an

urgent need to design Sn-based oxides with consistently high selectivity.

The electrocatalytic performance of Sn-based oxides can be promoted through compositional and structural engineering, which can tune the electrical properties and coordination stability of the active sites.<sup>16–19</sup> For instance, N doping had been conducted to regulate the charge density of the Sn active sites in SnO<sub>2</sub> to enhance the selectivity towards HCOO<sup>-</sup>.<sup>19</sup> Besides, SrSnO<sub>3</sub> has been proved to show high performance for the CO<sub>2</sub>RR to HCOO<sup>-</sup> as a result of the perovskite structure.<sup>16</sup> However, the stability of SrSnO<sub>3</sub> is still not satisfactory. The deactivation mechanism of such ABO<sub>3</sub> perovskite electrocatalysts was proposed to be the surface amorphization or reconstruction during the electrocatalytic processes.<sup>20–22</sup> Therefore, effective strategies to stabilize the crystal structures of perovskites would help further enhance the performance of Sn-based electrocatalysts. The insertion of rock-salt AO-layers in Ruddlesden–Popper (RP) perovskite not only induces interlayer interaction to stabilize the crystal structure, but also optimizes the electrical properties of the active B-site.<sup>23–26</sup>

This paper describes the design and synthesis of two-dimensional layered Sr<sub>2</sub>SnO<sub>4</sub> with a RP structure for the selective conversion of CO<sub>2</sub> to HCOO<sup>-</sup>. Compared with the SnO<sub>2</sub> and SrSnO<sub>3</sub> samples, Sr<sub>2</sub>SnO<sub>4</sub> shows enhanced selectivity with the Faradaic Efficiency (FE) for HCOO<sup>-</sup> reaching 83.7% (-1.08 V vs. the reversible hydrogen electrode). Besides, Sr<sub>2</sub>SnO<sub>4</sub> exhibits long-term stability for over 24 h. As revealed by the experiments and density functional theory (DFT) calculations, the SrO-layer in the RP structure is the key to achieving good performance,

<sup>a</sup>School of Chemical Engineering & Technology, Key Laboratory for Green Chemical Technology of Ministry of Education, Tianjin University, Tianjin 300072, China. E-mail: jlgong@tju.edu.cn

<sup>b</sup>Collaborative Innovation Center for Chemical Science & Engineering (Tianjin), Tianjin 300072, China

<sup>c</sup>Haihe Laboratory of Sustainable Chemical Transformations, Tianjin 300192, China

<sup>d</sup>Joint School of National University of Singapore and Tianjin University, International Campus of Tianjin University, Binhai New City, Fuzhou 350207, China

† Electronic supplementary information (ESI) available. See <https://doi.org/10.1039/d2sc03066g>

‡ These authors contributed equally to this work.



which could optimize the binding energy of \*OCHO and promote structural stability.

## Results and discussion

### Structures of catalysts

Fig. 1a shows the X-ray diffraction (XRD) patterns of SnO<sub>2</sub>, SrSnO<sub>3</sub>, and Sr<sub>2</sub>SnO<sub>4</sub>, the diffraction peaks of which are readily indexed to tetragonal SnO<sub>2</sub> (*P42mm*, JCPDS No. 41-1445), cubic SrSnO<sub>3</sub> (*Pm3m*, JCPDS No. 74-1298) and tetragonal Sr<sub>2</sub>SnO<sub>4</sub> (*I4/mmm*, JCPDS No. 97-002-7114), respectively. No peak corresponding to other phases was detected, demonstrating the high phase purity of SnO<sub>2</sub>, perovskite SrSnO<sub>3</sub>, and RP perovskite Sr<sub>2</sub>SnO<sub>4</sub> catalysts. The scanning electron microscopy (SEM) images reveal the porous structures of the samples (Fig. S1†). In addition, the electron dispersive X-ray spectroscopy (EDS) mappings exhibit uniform distributions of Sr, Sn, and O elements (Fig. S2 and S3†). To further confirm the formation of the RP phase, the high-resolution transmission electron microscopy (HRTEM) image of Sr<sub>2</sub>SnO<sub>4</sub> was collected (Fig. 1b). The observed lattice fringes with a spacing of 0.28 nm and 0.20 nm correspond to the (110) and (200) planes of Sr<sub>2</sub>SnO<sub>4</sub>. The inset shows the result of fast Fourier transform (FFT) analysis of the HRTEM image, which further confirms the tetragonal structure of Sr<sub>2</sub>SnO<sub>4</sub>. Moreover, the selected area electron diffraction (SAED) pattern of Sr<sub>2</sub>SnO<sub>4</sub> clearly reflects the tetragonally arranged diffraction spots of the [001] zone axes (Fig. 1c), consistent with the result of the HRTEM characterization.

Raman spectroscopy was used to investigate the differences in structures between the three Sn-based oxides (Fig. 1d). The bands centered at 472, 631 and 771 cm<sup>-1</sup> of SnO<sub>2</sub> correspond to the vibration modes of E<sub>g</sub>, A<sub>1g</sub>, and B<sub>2g</sub>, respectively.<sup>27</sup> The band of SrSnO<sub>3</sub> at 399 cm<sup>-1</sup> corresponds to SnO<sub>3</sub> torsional mode, and the peak at 576 cm<sup>-1</sup> is associated with Sn–O stretching vibrations, indicating the formation of [SnO<sub>6</sub>] octahedra.<sup>28,29</sup> The band of Sr<sub>2</sub>SnO<sub>4</sub> located at 445 cm<sup>-1</sup> is related to the vibration

of the bridge Sr–O–Sn oxygen bond axis in A<sub>1g</sub> symmetry along the *c* axis. This band shows the interactions between the perovskite layers and the rock-salt SrO-layers in the RP structure.<sup>30</sup> The differences in the crystal structures of the three oxides are illustrated in Fig. 1e. For SrSnO<sub>3</sub>, Sr<sup>2+</sup> ions occupy the A-sites, whereas Sn<sup>4+</sup> ions form the corner-linked [SnO<sub>6</sub>] octahedra at the B-sites. Sr<sub>2</sub>SnO<sub>4</sub> is composed of rock-salt SrO-layers and SrSnO<sub>3</sub> perovskite layers along the crystallographic *c*-axis direction. This alternating layered RP structure would lead to unique structural and electrical properties, which could be beneficial for promoting electrocatalytic performance.<sup>31,32</sup>

### CO<sub>2</sub>RR performance

The CO<sub>2</sub>RR performance was measured in a three-electrode H-type cell, with CO<sub>2</sub>-saturated 0.5 M KHCO<sub>3</sub> as electrolyte. The products were analysed at potentials between –0.88 and –1.28 V vs. the reversible hydrogen electrode (RHE). All the following potentials are referred to the RHE. Sr<sub>2</sub>SnO<sub>4</sub> exhibits a stable current density of up to 30.0 mA cm<sup>-2</sup> at –1.28 V, surpassing those of the SrSnO<sub>3</sub> (22.9 mA cm<sup>-2</sup>) and the SnO<sub>2</sub> (17.8 mA cm<sup>-2</sup>) electrocatalysts (Fig. S4a, S5a, and S6†). The FE for HCOO<sup>-</sup> against potential over Sr<sub>2</sub>SnO<sub>4</sub> shows a volcano trend, which first increases from 46.5% at –0.88 V to a peak value of 83.7% at –1.08 V. It then decreases to 62.7% at –1.28 V (Fig. 2a). The FEs for HCOO<sup>-</sup> over SnO<sub>2</sub> and SrSnO<sub>3</sub> also show similar volcano trends (Fig. S4b and S5b†), but with much lower peak values (64.6% for SrSnO<sub>3</sub> and 58.9% for SnO<sub>2</sub>). Besides, Sr<sub>2</sub>SnO<sub>4</sub> also exhibits the highest HCOO<sup>-</sup> partial current density of 12.4 mA cm<sup>-2</sup> at –1.08 V compared to SrSnO<sub>3</sub> (9.0 mA cm<sup>-2</sup>) and SnO<sub>2</sub> (5.9 mA cm<sup>-2</sup>) (Fig. S7†). The stability tests were performed at a consistent potential of –1.08 V (Fig. 2c). Sr<sub>2</sub>SnO<sub>4</sub> displays no obvious decay in the current density with the FE for HCOO<sup>-</sup> maintained at about 79.0%. However, there is an obvious increase in the current density for SrSnO<sub>3</sub> and SnO<sub>2</sub>, with a decrease in HCOO<sup>-</sup> FE at the same time. Although the

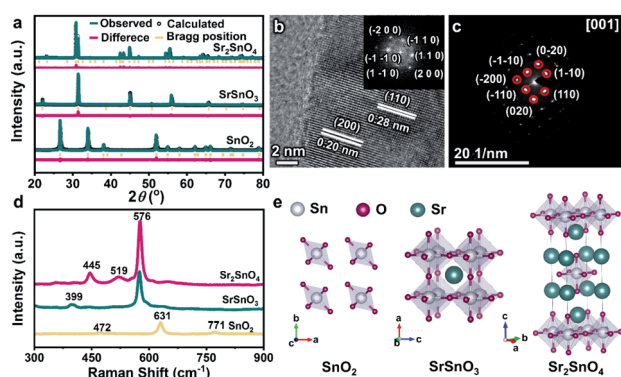


Fig. 1 (a) The XRD patterns of SnO<sub>2</sub>, SrSnO<sub>3</sub>, and Sr<sub>2</sub>SnO<sub>4</sub> with their Rietveld refinement results. (b) HRTEM and FFT (inset) images of Sr<sub>2</sub>SnO<sub>4</sub>. (c) The SAED patterns along [001] of Sr<sub>2</sub>SnO<sub>4</sub>. (d) The Raman spectra of SnO<sub>2</sub>, SrSnO<sub>3</sub>, and Sr<sub>2</sub>SnO<sub>4</sub>. (e) Illustrations of the crystal structures of SnO<sub>2</sub>, SrSnO<sub>3</sub>, and Sr<sub>2</sub>SnO<sub>4</sub>. Color code: O (purple), Sr (turquoise), and Sn (gray).

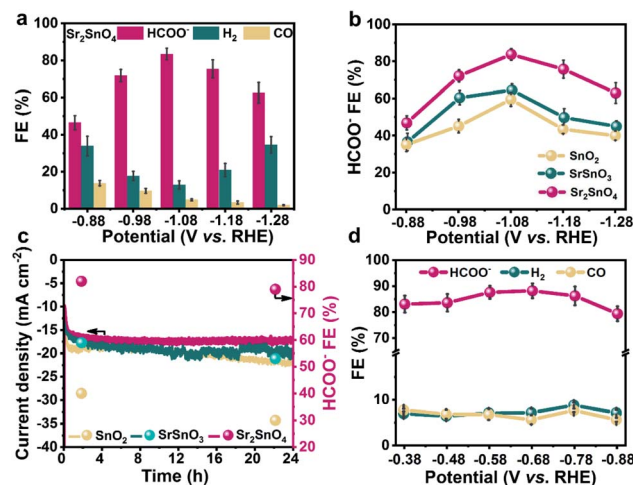


Fig. 2 (a) FEs for various products over Sr<sub>2</sub>SnO<sub>4</sub>. (b) FEs for HCOO<sup>-</sup> over SnO<sub>2</sub>, SrSnO<sub>3</sub> and Sr<sub>2</sub>SnO<sub>4</sub> at different potentials. (c) Stability tests of SnO<sub>2</sub>, SrSnO<sub>3</sub> and Sr<sub>2</sub>SnO<sub>4</sub> at a potential of –1.08 V vs. RHE. (d) FEs for various products over Sr<sub>2</sub>SnO<sub>4</sub> in a flow cell.



selectivity of these Sn-based electrocatalysts may not reach the high value reported in some representative studies,<sup>33,34</sup> the comparison of their performance could reflect the structural advantages of the RP perovskite. The electrocatalytic performance of Sr<sub>2</sub>SnO<sub>4</sub> was also evaluated in a flow cell with the catalysts dispersed on a gas diffusion electrode (GDE) to enhance the mass transfer of CO<sub>2</sub>. The peak FE towards HCOO<sup>-</sup> over Sr<sub>2</sub>SnO<sub>4</sub> is 84.5% at -0.68 V (Fig. 2d), and the current density for HCOO<sup>-</sup> reaches about 79.2 mA cm<sup>-2</sup> at -0.88 V (Fig. S8†). Moreover, Sr<sub>2</sub>SnO<sub>4</sub> displays long-term stability for over 50 h with the HCOO<sup>-</sup> partial current density maintained at about 59.1 mA cm<sup>-2</sup> (Fig. S9†). The electrolyte was replaced during the chronoamperometric test to avoid the formation of (bi)carbonate salts on the diffusion layer, which caused the strong fluctuation of current density. The FEs towards H<sub>2</sub> and CO are below 10.0% with negligible change. According to the results of the activity evaluation, the Sr<sub>2</sub>SnO<sub>4</sub> with the RP perovskite structure achieved consistently high selectivity towards HCOO<sup>-</sup>. The performance of Sr<sub>2</sub>SnO<sub>4</sub> is comparable to some of the state-of-the-art electrocatalysts for HCOO<sup>-</sup> production through the CO<sub>2</sub>RR (Table S1†).

### Operando Raman and ATR-SEIRAS spectra

To reveal the origin of the high stability of Sr<sub>2</sub>SnO<sub>4</sub>, *operando* Raman spectra of different samples were collected using a homemade electrochemical cell (Fig. S10†). With the decrease of the potential from -0.58 V to -1.28 V, the A<sub>1g</sub> peak of crystalline SnO<sub>2</sub> at 631 cm<sup>-1</sup> declines in intensity, which finally disappears after -1.08 V (Fig. 3a). This phenomenon would be caused by the reduction of SnO<sub>2</sub> to metallic Sn at high cathodic potentials, as proved by the formation of the Sn phase after the CO<sub>2</sub>RR stability test (Fig. S11a†).<sup>14</sup> In the *operando* Raman spectra of SrSnO<sub>3</sub>, the appearance of peaks at 631 cm<sup>-1</sup> below -1.08 V suggests the surface reconstruction of SrSnO<sub>3</sub> to form SnO<sub>2</sub> during the CO<sub>2</sub>RR, which would then be partially reduced to metallic Sn (Fig. 3b). This result could be supported by the XRD pattern of SrSnO<sub>3</sub> after the stability test, which clearly shows the presence of SnO<sub>2</sub> and Sn phases (Fig. S11b†).<sup>16</sup> In contrast, the Raman bands of Sr<sub>2</sub>SnO<sub>4</sub> at 445 cm<sup>-1</sup> arising from the interactions between the perovskite layer and rock-salt SrO-layer remain unchanged at different potentials, same as the bands corresponding to the [SnO<sub>6</sub>] octahedra at 576 cm<sup>-1</sup>

(Fig. 3c). These phenomena are in agreement with the end-of-test XRD pattern, showing diffraction peaks of only Sr<sub>2</sub>SnO<sub>4</sub> (Fig. S11c†). The HRTEM and SEM images of the three Sn-based oxide catalysts after the CO<sub>2</sub>RR stability test have been characterized. There was a significant change in the morphology of SnO<sub>2</sub> (Fig. S12a†). Such a change could be ascribed to the reduction of SnO<sub>2</sub> to metallic Sn (Fig. S13†). Similar phenomena could also be found for SrSnO<sub>3</sub>, which could be reduced to SnO<sub>2</sub> and Sn (Fig. S12b and S14†). However, the morphology of the Sr<sub>2</sub>SnO<sub>4</sub> electrocatalyst was maintained after the CO<sub>2</sub>RR stability test (Fig. S12c†). Besides, the HRTEM image showed that the crystalline nature of Sr<sub>2</sub>SnO<sub>4</sub> was maintained (Fig. S15†). EDS mappings of Sr<sub>2</sub>SnO<sub>4</sub> after the stability test exhibit uniform distributions of Sr, Sn, and O elements (Fig. S16†). The results above demonstrate the superior stability of Sr<sub>2</sub>SnO<sub>4</sub> during the CO<sub>2</sub>RR. The high durability of Sr<sub>2</sub>SnO<sub>4</sub> would be induced by the SrO-layer insertion in the RP structure, which leads to the strong interaction between perovskite layers and rock-salt SrO-layers to prohibit structural deformation and reconstruction.<sup>26</sup>

In addition to good stability, the RP perovskite Sr<sub>2</sub>SnO<sub>4</sub> electrocatalyst shows high selectivity towards HCOO<sup>-</sup>. To find the underlining mechanism of the promoted electrocatalytic performance, *operando* attenuated-total-reflection surface-enhanced infrared absorption spectroscopy (ATR-SEIRAS) characterization was conducted. The peaks at around 1630 cm<sup>-1</sup> observed in all three samples can be assigned to the interfacial H<sub>2</sub>O (Fig. 4a-c).<sup>9,35</sup> The bands at 1367–1358 cm<sup>-1</sup>, 1397–1390 cm<sup>-1</sup> and 1390–1386 cm<sup>-1</sup> for SnO<sub>2</sub>, SrSnO<sub>3</sub> and Sr<sub>2</sub>SnO<sub>4</sub> with an obvious Stark effect (peak position shifted to a lower wavenumber at more negative potentials) could be assigned to \*OCHO adsorbed on the surface.<sup>36,37</sup> The \*OCHO peaks of SnO<sub>2</sub> can be observed from -0.48 V to -1.28 V. For SrSnO<sub>3</sub>, the signal of \*OCHO appears at -0.68 V and disappears at -1.18 V. The signal of \*OCHO was detected from -0.58 V to -0.88 V for Sr<sub>2</sub>SnO<sub>4</sub>. Since \*OCHO is the essential intermediate for the generation of HCOO<sup>-</sup>,<sup>38</sup> its rapid desorption on Sr<sub>2</sub>SnO<sub>4</sub> would be the result of the weak adsorption of \*OCHO, considering its high selectivity towards HCOO<sup>-</sup>.<sup>39,40</sup> Therefore, the high selectivity of Sr<sub>2</sub>SnO<sub>4</sub> would originate from the optimized binding energy of \*OCHO on the surface, which might be realized by the SrO-layer insertion in the RP perovskite structure.

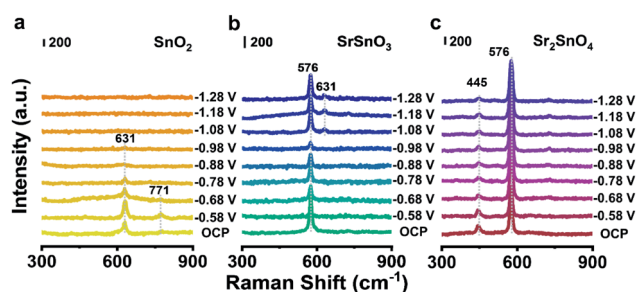


Fig. 3 *Operando* Raman spectra of (a) SnO<sub>2</sub>, (b) SrSnO<sub>3</sub> and (c) Sr<sub>2</sub>SnO<sub>4</sub> recorded at various potentials vs. RHE in a CO<sub>2</sub>-saturated 0.5 M KHCO<sub>3</sub> solution, respectively.

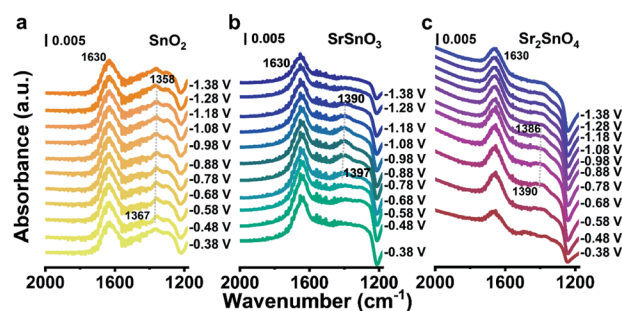


Fig. 4 *Operando* ATR-SEIRAS spectra of (a) SnO<sub>2</sub> (b) SrSnO<sub>3</sub> and (c) Sr<sub>2</sub>SnO<sub>4</sub> recorded at various potentials vs. RHE in a CO<sub>2</sub>-saturated 0.5 M KHCO<sub>3</sub> solution, respectively.



## DFT simulations

To further reveal the intrinsic role of the RP structure of  $\text{Sr}_2\text{SnO}_4$  in promoting selectivity, DFT simulations were performed. Thermodynamically stable  $\text{SnO}_2(110)$ ,<sup>41</sup>  $\text{SrSnO}_3(001)$  (Table S2†) and SrO-terminated  $\text{Sr}_2\text{SnO}_4(002)$  surfaces<sup>24</sup> were chosen as the starting models for the computational study. The influence of surface vacancies, which significantly affect the surface catalytic reactions, was considered due to the relatively large energy required for the formation of bulk oxygen vacancies in these samples (Tables S3 and S4†). According to their surface phase diagrams (Fig. S17†),  $\text{SnO}_2(110)/4\text{O}_{\text{br}}\text{H}^*$ ,<sup>41</sup>  $\text{SrSnO}_3(001)/7\text{Ov}$  and  $\text{Sr}_2\text{SnO}_4(002)/8\text{Ov}$  were found to be stable in the  $\text{CO}_2\text{RR}$  process. These models were selected for the understanding of the reaction mechanism, which would represent the real active sites of the catalysts during the reaction. As shown in the well-discussed reaction pathway of the  $\text{CO}_2\text{RR}$  to  $\text{HCOO}^-$  (Fig. S18†), the  $^*\text{OCHO}$  intermediate is formed by the hydrogenation of  $\text{CO}_2$ , which subsequently produces  $\text{HCOOH}$  by the transfer of electrons and protons.<sup>41,42</sup> The results of DFT simulations show that the formation energy of  $^*\text{OCHO}$  over the  $\text{Sr}_2\text{SnO}_4(002)/8\text{Ov}$  surface (0.20 eV) is higher than those over the  $\text{SrSnO}_3(001)/7\text{Ov}$  and the  $\text{SnO}_2(110)$  (Fig. 5a). The process of  $^*\text{OCHO}$  desorption to form  $\text{HCOOH}$  on  $\text{Sr}_2\text{SnO}_4(002)/8\text{Ov}$  is spontaneous. However, the energy barriers for  $^*\text{OCHO}$  desorption over  $\text{SnO}_2(110)$  and  $\text{SrSnO}_3(001)/7\text{Ov}$  are around 0.70 eV and 0.39 eV. Therefore,  $\text{Sr}_2\text{SnO}_4$  undergoes easy desorption of  $^*\text{OCHO}$  for the  $\text{CO}_2\text{RR}$  to  $\text{HCOO}^-$ , which is in accordance with the results of the *operando* ATR-SEIRAS characterization. Besides, the  $\Delta G_{\text{H}^*}$  on  $\text{Sr}_2\text{SnO}_4(002)/8\text{Ov}$  is higher than those on the  $\text{SrSnO}_3(001)/7\text{Ov}$  and the  $\text{SnO}_2(110)$  (Fig. 5b), as reflected by the relatively low selectivity towards  $\text{H}_2$  on  $\text{Sr}_2\text{SnO}_4$  (Fig. 2a, S4b and S5b†). Since the thermodynamically stable SrO-layer in  $\text{Sr}_2\text{SnO}_4(002)$  may be involved in the reaction (Fig. S19†), its role in the  $\text{CO}_2\text{RR}$  was investigated, which would also promote  $^*\text{OCHO}$  generation

and inhibit  $\text{H}_2$  production (Fig. S20†). These results indicate that  $\text{Sr}_2\text{SnO}_4$  exhibits high selectivity due to the optimized binding strength of  $^*\text{OCHO}$ .

Furthermore, crystal orbital Hamilton population (COHP) analysis was conducted to explore how the SrO-layer insertion in  $\text{Sr}_2\text{SnO}_4$  would affect the selectivity (Fig. 5c). The anti-bonding orbitals of Sn active sites with the O atom of  $^*\text{OCHO}$  below the Fermi level ( $E_f$ ) imply the weakening adsorption of  $^*\text{OCHO}$  on Sn, which is most obvious on the  $\text{Sr}_2\text{SnO}_4(002)$  surface. Therefore, the filling of the anti-bonding orbitals leads to a reduction in the bonding strength of Sn–O, corresponding to the relatively weak adsorption strength of  $^*\text{OCHO}$  on  $\text{Sr}_2\text{SnO}_4$ . Besides, the linear relationship between the integrated COHP (iCOHP) and  $\Delta G_{^*\text{OCHO}}$  quantitatively confirms that the population of bonding/antibonding orbitals below  $E_f$  is the key factor in regulating the  $\Delta G_{^*\text{OCHO}}$  (Fig. 5d).<sup>41</sup> Therefore, the tuned electrical properties of active sites in the RP perovskite  $\text{Sr}_2\text{SnO}_4$  electrocatalyst optimize the binding energy of  $^*\text{OCHO}$  over  $\text{Sr}_2\text{SnO}_4(002)/8\text{Ov}$ , leading to the high selectivity for the  $\text{CO}_2\text{RR}$  to  $\text{HCOO}^-$ .

## Conclusions

In summary, a  $\text{Sr}_2\text{SnO}_4$  perovskite electrocatalyst with a RP structure was fabricated *via* a simple solid-state reaction.  $\text{Sr}_2\text{SnO}_4$  exhibits high performance for the  $\text{CO}_2\text{RR}$  with an FE of 83.7% towards  $\text{HCOO}^-$  and long-term durability of over 24 h. The SrO-layer insertion in the RP structure leads to strong interlayer interactions, which could prohibit structural deformation and reconstruction. Thus,  $\text{Sr}_2\text{SnO}_4$  possesses good stability. Besides, the anti-bonding orbital filling of the Sn active site in the RP structure results in the favorable binding strength of  $^*\text{OCHO}$  on  $\text{Sr}_2\text{SnO}_4$ , so that it shows higher selectivity towards  $\text{HCOO}^-$  than the  $\text{SnO}_2$  and the  $\text{SrSnO}_3$  control samples. Our work demonstrates that  $\text{Sr}_2\text{SnO}_4$  can serve as an efficient electrocatalyst for  $\text{HCOO}^-$  production through the  $\text{CO}_2\text{RR}$ . The findings would guide the rational design of perovskite-based electrocatalysts and open up an avenue for tuning the catalytic selectivity and stability by structure engineering.

## Data availability

The data that supports the findings of this study is available from the corresponding author upon reasonable request.

## Author contributions

J. L. G supervised the project. P. Z. and J. Z. conceived the idea. J. Z. synthesized the catalysts and conducted the  $\text{CO}_2\text{RR}$  performance tests. L. L. L conducted DFT simulations. Y. T. H., G. H., and G. Z. conducted related characterization studies. All the authors participated in the writing of the manuscript.

## Conflicts of interest

There are no conflicts to declare.

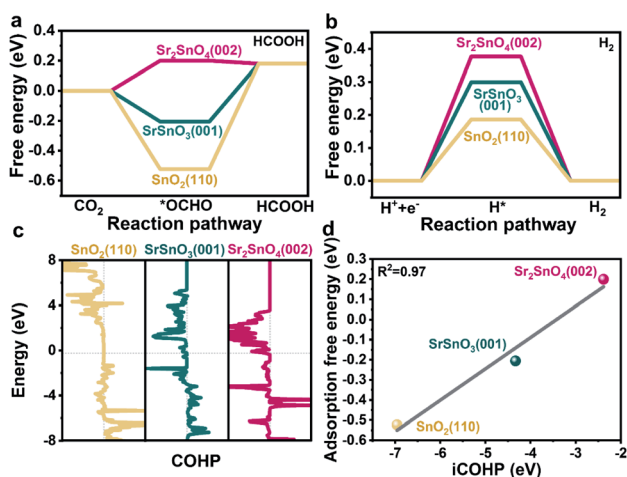


Fig. 5 The calculated free energy for (a)  $\text{HCOOH}$  and (b)  $\text{H}_2$ . (c) COHP curves of Sn active sites on  $\text{SnO}_2(110)$ ,  $\text{SrSnO}_3(001)$ , and  $\text{Sr}_2\text{SnO}_4(002)$  with O of  $^*\text{OCHO}$  interaction. (d) The correlation between the iCOHP and adsorption free energy of  $^*\text{OCHO}$  on  $\text{SnO}_2(110)$ ,  $\text{SrSnO}_3(001)$ , and  $\text{Sr}_2\text{SnO}_4(002)$ .



## Acknowledgements

We acknowledge the National Key R&D Program of China (2021YFA1501503), the National Natural Science Foundation of China (22121004, 22108197), the Haihe Laboratory of Sustainable Chemical Transformations (CYZC202107), the Natural Science Foundation of Tianjin City (18JJCQJC47500), the Program of Introducing Talents of Discipline to Universities (No. BP0618007) and the Xplorer Prize for financial support.

## References

- 1 S. Zhang, Q. Fan, R. Xia and T. J. Meyer, *Acc. Chem. Res.*, 2020, **53**, 255–264.
- 2 X. Wang, Z. Wang, F. P. García de Arquer, C.-T. Dinh, A. Ozden, Y. Li, D.-H. Nam, J. Li, Y.-S. Liu, J. Wicks, Z. Chen, M. Chi, B. Chen, Y. Wang, J. Tam, J. Y. Howe, A. Proppe, P. Todorović, F. Li, T.-T. Zhuang, C. M. Gabardo, A. R. Kirmani, C. McCallum, S.-F. Hung, Y. Lum, M. Luo, Y. Min, A. Xu, C. P. O'Brien, B. Stephen, B. Sun, A. H. Ip, L. J. Richter, S. O. Kelley, D. Sinton and E. H. Sargent, *Nat. Energy*, 2020, **5**, 478–486.
- 3 Y. Ling, Q. Ma, Y. Yu and B. Zhang, *Trans. Tianjin Univ.*, 2021, **27**, 180–200.
- 4 X. An, S. Li, X. Hao, Z. Xie, X. Du, Z. Wang, X. Hao, A. Abudula and G. Guan, *Renew. Sustain. Energy Rev.*, 2021, **143**, 110952.
- 5 N. Han, P. Ding, L. He, Y. Li and Y. Li, *Adv. Energy Mater.*, 2020, **10**, 1902338.
- 6 S. Agarwal, Y. Zhai, D. Hill and N. Sridhar, *ChemSusChem*, 2011, **4**, 1301–1310.
- 7 Y. Chen and M. W. Kanan, *J. Am. Chem. Soc.*, 2012, **134**, 1986–1989.
- 8 R. Daiyan, E. C. Lovell, N. M. Bedford, W. H. Saputera, K.-H. Wu, S. Lim, J. Horlyck, Y. H. Ng, X. Lu and R. Amal, *Adv. Sci.*, 2019, **6**, 1900678.
- 9 W. Deng, L. Zhang, L. Li, S. Chen, C. Hu, Z.-J. Zhao, T. Wang and J. Gong, *J. Am. Chem. Soc.*, 2019, **141**, 2911–2915.
- 10 H. Li, N. Xiao, Y. Wang, C. Liu, S. Zhang, H. Zhang, J. Bai, J. Xiao, C. Li, Z. Guo, S. Zhao and J. Qiu, *J. Mater. Chem. A*, 2020, **8**, 1779–1786.
- 11 S. Lee, H. Ju, R. Machunda, S. Uhm, J. K. Lee, H. J. Lee and J. Lee, *J. Mater. Chem. A*, 2015, **3**, 3029–3034.
- 12 N. Han, Y. Wang, J. Deng, J. Zhou, Y. Wu, H. Yang, P. Ding and Y. Li, *J. Mater. Chem. A*, 2019, **7**, 1267–1272.
- 13 C. Liang, B. Kim, S. Yang, Y. Liu, C. F. Woellner, Z. Li, R. Vajtai, W. Yang, J. Wu, P. J. A. Kenis and P. M. Ajayan, *J. Mater. Chem. A*, 2018, **6**, 10313–10319.
- 14 A. Dutta, A. Kuzume, M. Rahaman, S. Vesztergom and P. Broekmann, *ACS Catal.*, 2015, **5**, 7498–7502.
- 15 R. Daiyan, X. Lu, Y. H. Ng and R. Amal, *Catal. Sci. Technol.*, 2017, **7**, 2542–2550.
- 16 Y. Pi, J. Guo, Q. Shao and X. Huang, *Nano Energy*, 2019, **62**, 861–868.
- 17 X. An, S. Li, A. Yoshida, T. Yu, Z. Wang, X. Hao, A. Abudula and G. Guan, *ACS Appl. Mater. Interfaces*, 2019, **11**, 42114–42122.
- 18 G. Wen, B. Ren, M. G. Park, J. Yang, H. Dou, Z. Zhang, Y.-P. Deng, Z. Bai, L. Yang, J. Gostick, G. A. Botton, Y. Hu and Z. Chen, *Angew. Chem., Int. Ed.*, 2020, **59**, 12860–12867.
- 19 C. Hu, L. Zhang, L. Li, W. Zhu, W. Deng, H. Dong, Z.-J. Zhao and J. Gong, *Sci. China Chem.*, 2019, **62**, 1030–1036.
- 20 N. Tsvetkov, Q. Lu, L. Sun, E. J. Crumlin and B. Yildiz, *Nat. Mater.*, 2016, **15**, 1010–1016.
- 21 Y. Chen, H. Li, J. Wang, Y. Du, S. Xi, Y. Sun, M. Sherburne, J. W. Ager III, A. C. Fisher and Z. J. Xu, *Nat. Commun.*, 2019, **10**, 572.
- 22 X. Xu, Y. Chen, W. Zhou, Z. Zhu, C. Su, M. Liu and Z. Shao, *Adv. Mater.*, 2016, **28**, 6442–6448.
- 23 J. Wang, C. Cheng, B. Huang, J. Cao, L. Li, Q. Shao, L. Zhang and X. Huang, *Nano Lett.*, 2021, **21**, 980–987.
- 24 Y. Zhu, H. A. Tahini, Z. Hu, J. Dai, Y. Chen, H. Sun, W. Zhou, M. Liu, S. C. Smith, H. Wang and Z. Shao, *Nat. Commun.*, 2019, **10**, 149.
- 25 C. Zhu, H. Tian, B. Huang, G. Cai, C. Yuan, Y. Zhang, Y. Li, G. Li, H. Xu and M.-R. Li, *Chem. Eng. J.*, 2021, **423**, 130185.
- 26 L.-F. Huang, N. Z. Koocher, M. Gu and J. M. Rondinelli, *Chem. Mater.*, 2018, **30**, 7100–7110.
- 27 S. Sun, G. Meng, G. Zhang, T. Gao, B. Geng, L. Zhang and J. Zuo, *Chem. Phys. Lett.*, 2003, **376**, 103–107.
- 28 M. Muralidharan, V. Anbarasu, A. Elaya Perumal and K. Sivakumar, *J. Mater. Sci.: Mater. Electron.*, 2017, **28**, 4125–4137.
- 29 U. Kumar and S. Upadhyay, *J. Electron. Mater.*, 2019, **48**, 5279–5293.
- 30 A. Magrez, M. Cochet, O. Joubert, G. Louarn, M. Ganne and O. Chauvet, *Chem. Mater.*, 2001, **13**, 3893–3898.
- 31 R. P. Forslund, W. G. Hardin, X. Rong, A. M. Abakumov, D. Filimonov, C. T. Alexander, J. T. Mefford, H. Iyer, A. M. Kolpak, K. P. Johnston and K. J. Stevenson, *Nat. Commun.*, 2018, **9**, 3150.
- 32 G. Nirala, D. Yadav and S. Upadhyay, *J. Adv. Ceram.*, 2020, **9**, 129–148.
- 33 Y. Hori, H. Wakebe, T. Tsukamoto and O. Koga, *Electrochim. Acta*, 1994, **39**, 1833–1839.
- 34 K. Bejtka, J. Zeng, A. Sacco, M. Castellino, S. Hernández, M. A. Farkhondehfar, U. Savino, S. Ansaloni, C. F. Pirri and A. Chiodoni, *ACS Appl. Energy Mater.*, 2019, **2**, 3081–3091.
- 35 W. Thornton and P. G. Harrison, *J. Chem. Soc., Faraday Trans.*, 1975, **71**, 461–472.
- 36 Y. Katayama, F. Nattino, L. Giordano, J. Hwang, R. R. Rao, O. Andreussi, N. Marzari and Y. Shao-Horn, *J. Phys. Chem. C*, 2018, **123**, 5951–5963.
- 37 Y. Liang, W. Zhou, Y. Shi, C. Liu and B. Zhang, *Sci. Bull.*, 2020, **65**, 1547–1554.
- 38 J. E. Pander, M. F. Baruch and A. B. Bocarsly, *ACS Catal.*, 2016, **6**, 7824–7833.
- 39 S. Zhu, B. Jiang, W.-B. Cai and M. Shao, *J. Am. Chem. Soc.*, 2017, **139**, 15664–15667.
- 40 J. Heyes, M. Dunwell and B. Xu, *J. Phys. Chem. C*, 2016, **120**, 17334–17341.
- 41 L. Li, Z.-J. Zhao, C. Hu, P. Yang, X. Yuan, Y. Wang, L. Zhang, L. Moskaleva and J. Gong, *ACS Energy Lett.*, 2020, **5**, 552–558.
- 42 J. S. Yoo, R. Christensen, T. Vegge, J. K. Nørskov and F. Studt, *ChemSusChem*, 2016, **9**, 358–363.

